IJMSSSR

International Journal of Management studies and Social Science Research
A Bi-Monthly, Peer-Reviewed, Open-Access Journal

2026 Vol. 08, Issue 06
ISSN: 2582-0265
www.ijmsssr.org

RESEARCH ARTICLE

Forecast-Aware Adaptive Surplus Allocation for Interpretable Energy Management in Industrial-Park Multi-Energy Systems

JiYu Li, Bingqian Chen, Xue Chen

State Grid Fujian Electric Power Economic and Technological Research Institute, Fuzhou 350003, China

ABSTRACT

Industrial parks with high renewable-energy penetration require coordinated management of coupled electricity, heat, storage, and gas-conversion assets while preserving transparent operating logic. Rule-based controllers remain attractive for practical deployment because their decisions can be inspected and verified by operators. However, a fixed renewable-surplus priority cannot distinguish brief surplus events from sustained renewable generation and may therefore exhaust battery headroom prematurely. This study proposes forecast-aware residual-surplus allocation (FARSA), a lightweight extension of an interpretable coordinated rule that preserves the combined heat and power (CHP)–heat pump (HP) cooperative-heating logic while adapting only the allocation between the battery energy storage system (BESS) and power-to-gas (P2G). FARSA forecasts the residual renewable surplus remaining after HP use, compares discounted surplus energy with the remaining BESS charging headroom, and adjusts an explicit allocation threshold using state of charge and the anticipated electricity-price spread. The method is calibrated on an independent synthetic year, after which all parameters are fixed. On a full-year hourly synthetic benchmark, FARSA reduced renewable curtailment from 237.83 to 173.74 MWh, a 26.95% reduction relative to the static coordinated rule. Annual operating cost, net fossil-gas use, and CO2 emissions decreased by 0.126%, 0.128%, and 0.128%, respectively. Across six operating conditions and ten independent stochastic realizations, the blocked mean reductions were 33.43% for curtailment and 0.140% for operating cost. For both metrics, the Wilcoxon signed-rank test gave $p=0.0020$ and the Holm-adjusted value was $p=0.0078$. A measurement-driven transfer test using public Honda Research and Development (R&D) Europe facility data reduced 2023 curtailment from 3.96 to 2.23 MWh, while annual operating cost decreased by only 0.012% under the benchmark tariff. Counterfactual PV-capacity expansion tests retained a curtailment benefit but revealed small cost and emission trade-offs at higher PV penetration. The results indicate that FARSA is most useful when temporal allocation, rather than insufficient flexibility capacity, is the dominant operational bottleneck.

Keywords: *multi-energy system, interpretable control, battery storage, power-to-gas, forecast-aware rule, industrial energy management, measurement-driven validation*

ARTICLE INFO

Received: [30/09/2026]
Accepted: [08/10/2026]

Published: [05/11/2026]
Issue Period: November - December 2026 (Bi-Monthly)
DOI: https://doi.org/10.56293/IJMSSSR.2026.6501
Copyright: © 2026 The Author(s). Published by IJMSSSR. This is an Open Access article distributed under the terms and conditions of the Creative Commons Attribution (CC BY 4.0) License.

1. Introduction

Industrial parks increasingly combine distributed renewable generation with electricity, heat, storage, and gas-conversion assets. The multi-energy-system concept provides a system-level framework for describing these coupled carriers and conversion paths (Mancarella, 2014). Energy-flow studies have shown that coordination across networks can create operational synergies that are not visible from stand-alone device efficiencies (Badami & Fambri, 2019). The related energy-hub literature further emphasizes joint conversion and exchange among electricity, heat, and gas infrastructures (Mohammadi et al., 2017). These findings motivate dispatch strategies that evaluate devices according to their contribution to the coupled system rather than to a single energy stream.

Data-driven control has become an important complement to deterministic optimization for such systems. The Markov decision-process framework provides the standard mathematical basis for sequential reinforcement-learning decisions (Sutton & Barto, 2018). A broad review of reinforcement learning in energy systems documents its use in scheduling, building energy management, and renewable integration (Perera & Kamalaruban, 2021). Deep deterministic policy gradient enables actor–critic learning directly in continuous action spaces (Lillicrap et al., 2015). Twin-delayed actor–critic learning reduces value overestimation and improves training stability for continuous control (Fujimoto et al., 2018). In energy applications, reinforcement learning has been used to schedule battery storage according to load and price variations (Abedi et al., 2022). It has also been applied to intelligent economic dispatch of combined heat and power systems (Zhou et al., 2020). Real-time microgrid energy management under uncertainty provides another representative application (Guo et al., 2022). Related work on combined cooling, heating, and power systems has further demonstrated the potential of deep reinforcement learning for coordinated operation with storage and renewable generation (Ruan et al., 2023). However, neural-network policies remain difficult to audit, explain, and translate into plant operating procedures.

Interpretability is especially important in industrial energy management, where operators must understand why a device is activated and whether a decision respects process constraints. A systematic review of data-driven residential and industrial energy management highlights both the opportunities of learning-based methods and the need for deployable decision support (Sievers & Blank, 2023). Open Power System Data provides reproducible time series for load, renewable generation, and electricity markets that are widely used for energy-system studies (Open Power System Data, 2020). Public heat-demand and heat-pump-efficiency time series provide an additional basis for reproducible thermal-system modeling (Ruhnau et al., 2019). These open resources are useful for model development, but they do not by themselves provide a complete, synchronized industrial-park trajectory containing all electricity, heat, storage, and P2G states required by the present controller.

The allocation between BESS and P2G is a particularly relevant operational problem because the two technologies provide flexibility on different time scales. Recent hierarchical energy-management research for hybrid battery and P2G systems shows that coordinated operation can improve renewable-energy utilization across multiple services (Biermann & Bocklisch, 2026). Earlier hybridization studies likewise demonstrate that battery storage and P2G play complementary roles in renewable-energy systems and that their interaction influences system-level performance (Gillessen et al., 2017). For measurement-driven transfer evaluation, this study uses a real-world energy-management dataset from the Honda Research and Development (R&D) Europe facility, which provides measured industrial electricity, heat, on-site generation, and meteorological trajectories (Engel et al., 2025a). The associated public repository provides the measurements at multiple temporal resolutions and supports reproducible analysis (Engel et al., 2025b).

The starting point for the present study is a fully explicit coordinated rule that combines a CHP–HP cooperative-heating mechanism with a fixed renewable-surplus priority. The rule is used as an interpretable operational baseline rather than as a proxy for a neural policy, and all control actions evaluated in this paper are generated by deterministic logic specified below. A residual limitation remains: renewable surplus is processed in a fixed sequence in which the HP is served first, the BESS is charged second, and P2G is activated last. This sequence is transparent, but it does not distinguish a brief surplus pulse from a sustained renewable event. If the BESS is filled too early during a long surplus interval, a subsequent renewable peak can encounter both a nearly full battery and a power-limited P2G unit, increasing curtailment. Conversely, diverting every short surplus pulse to P2G can reduce the stored electricity available for later high-value discharge.

This paper addresses that narrow gap through forecast-aware residual-surplus allocation (FARSA). FARSA retains the original CHP–HP cooperative-heating rule and modifies only the allocation between BESS and P2G after the HP has absorbed the immediately useful renewable surplus. The method estimates discounted post-HP surplus over a short forecast horizon, compares it with input-side BESS headroom, and adjusts a transparent allocation threshold according to SOC and future electricity-price value. The resulting control action remains explicit and auditable and does not require an online optimization problem.

The evaluation is designed to separate methodological validity, robustness, transferability, and idealized optimization potential. FARSA parameters are determined on an independent calibration year and then frozen. Statistical inference uses independent stochastic realizations as sampling units instead of treating scenario variants derived from the same underlying realization as independent observations. Perfect-foresight references use the same physical energy paths and objective-consistent comparisons as the rule simulator. Finally, the frozen rule is replayed on measured Honda facility trajectories without retuning. This design identifies when a lightweight, explainable rule can capture useful flexibility and when capacity expansion or system-level optimization remains necessary.

The study makes three contributions. First, it introduces a forecast-aware and physically interpretable BESS–P2G allocation rule based on post-HP surplus, battery headroom, state of charge, and future price value. Second, it evaluates the rule with independent calibration, paired multi-scenario tests, blocked statistical inference, and objective-consistent perfect-foresight references. Third, it tests transfer to measured industrial-facility trajectories while explicitly separating measured exogenous data from counterfactual BESS, P2G, and PV-capacity assumptions.

2. System Model and Baseline Control

2.1 Energy-system structure

The simulated industrial-park multi-energy system contains photovoltaic (PV) and wind generation, an external electricity grid, a CHP unit, a BESS, a centralized HP, a gas boiler (GB), and a P2G process. Renewable electricity first serves the electrical load. The BESS provides short-term shifting, the CHP couples gas with electricity and heat, the HP converts electricity into heat, P2G converts residual electricity into synthetic natural gas (SNG) and recoverable heat, and the GB supplies the remaining thermal deficit. The external electricity and gas networks are treated as open boundaries. The model is hourly and quasi-steady-state. Start-up behavior, ramping, minimum stable load, and network transport dynamics are outside the present scope.

$$P_{net}(t) = P_{load}(t) - P_{RES}(t), \qquad P_{RES}(t) = P_{PV}(t) + P_{WT}(t) \tag{1}$$

$$SOC(t+1) = SOC(t) + \frac{\eta_c P_{ch}(t)\Delta t}{E_B} - \frac{P_{dis}(t)\Delta t}{\eta_d E_B} \tag{2}$$

$$E_{SNG}(t) = \eta_{P2G} P_{P2G}(t)\Delta t, \qquad E_{rec}(t) = \kappa_h P_{P2G}(t)\Delta t \tag{3}$$

2.2 Static coordinated rule

The baseline deterministic rule uses a fixed renewable-surplus order. When renewable generation exceeds electrical demand, the HP is supplied first, followed by BESS charging and then P2G. Any remaining electricity is curtailed. During an electricity deficit, the BESS discharges first, followed by CHP generation and external-grid import. Thermal demand is satisfied by the HP, usable P2G heat, CHP heat, and finally the GB.

The static coordinated rule retains the same priority and incorporates a CHP–HP cooperative-heating mechanism. If the CHP is already operating, heat demand remains unsatisfied, and both the CHP and HP have headroom, CHP electrical output is increased and the additional electricity is routed directly to the HP. For an incremental CHP electrical power ΔP_{CHP}, the associated heating increment is

$$\Delta Q_{coop}(t) = \left[\frac{\eta_h}{\eta_e} + COP(t)\right]\Delta P_{CHP}(t) \tag{4}$$

Thus, the same incremental gas input produces both CHP heat and HP heat. FARSA leaves this rule unchanged and modifies only the allocation between BESS and P2G after the HP has absorbed the immediately useful renewable surplus.

3. Proposed FARSA Method

The complete decision flow is summarized in Figure 1. FARSA is inserted after the CHP–HP cooperative-heating decision and before final BESS–P2G routing, so the baseline thermal coordination logic remains unchanged.

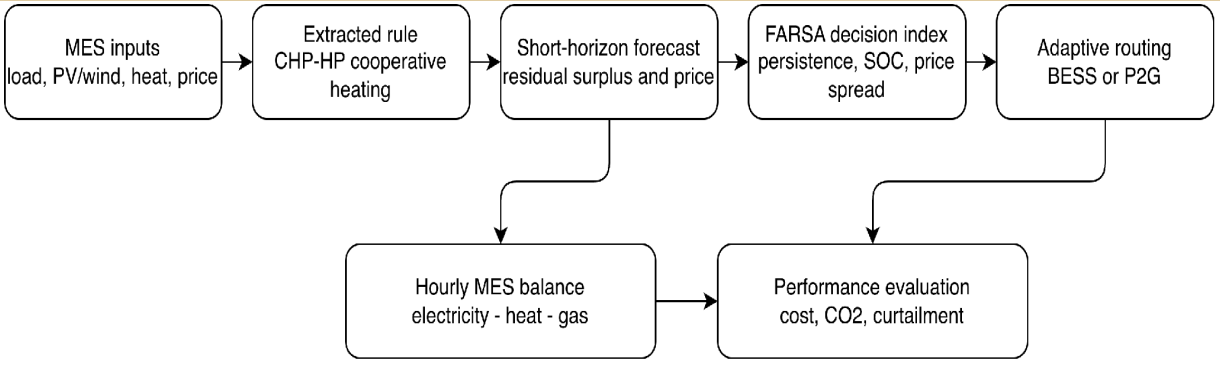


Figure 1. FARSA framework embedded in the interpretable rule controller.

3.1 Post-HP surplus forecast

At decision time t, let the forecast horizon contain H hourly steps of renewable generation, electrical demand, heat demand, heat-pump coefficient of performance, and electricity price. The predicted renewable surplus at a future step $t + k$ is

$$\hat{P}_{sur,0}(t + k) = \left[\hat{P}_{RES}(t + k) - \hat{P}_{load}(t + k)\right]_{+} \tag{5}$$

The predicted HP electricity that can be directly supplied by renewable surplus is limited jointly by available surplus, the HP thermal rating, and predicted heat demand:

$$\hat{P}_{HP,RES}(t + k) = min\left\{\hat{P}_{sur,0}(t + k), \frac{Q_{HP,max}}{COP_f(t+k)}, \frac{\hat{Q}_{dem}(t+k)}{COP_f(t+k)}\right\} \tag{6}$$

The quantity relevant to BESS–P2G allocation is therefore the predicted surplus remaining after HP absorption rather than the gross difference between renewable generation and electrical demand:

$$\hat{S}(t + k) = \hat{P}_{sur,0}(t + k) - \hat{P}_{HP,RES}(t + k) \tag{7}$$

Near-term forecasts are assigned greater weight using the discount factor $\gamma = 0.90$. The resulting cumulative post-HP surplus energy is

$$E^{H}_{sur}(t) = \Delta t \sum_{k=0}^{H-1} \gamma^{k} \hat{S}(t + k) \tag{8}$$

3.2 Input-side BESS headroom and dynamic threshold

To preserve a physically interpretable ratio, the BESS denominator is expressed as the input-side electricity that can still be accepted, including charging efficiency:

$$E^{in}_{free}(t) = \frac{E_B\left[SOC_{max} - SOC(t)\right]}{\eta_c} \tag{9}$$

$$R(t) = \frac{E^{H}_{sur}(t)}{max\left\{E^{in}_{free}(t), \varepsilon_{E}\right\}} \quad (10)$$

A headroom floor of $\varepsilon_E = 0.25$ MWh is used to prevent numerical instability when the battery approaches its upper state-of-charge limit. This safeguard does not modify the physical BESS capacity constraint.

A value of $R(t) \approx 1$ indicates that the discounted future post-HP surplus is comparable with the remaining input-side battery headroom. Larger values of $R(t)$ indicate a greater risk that immediate BESS charging will reduce the capacity available to absorb subsequent renewable peaks.

Battery value also depends on SOC and the opportunity to discharge at a higher future electricity price. FARSA therefore uses

$$\Theta(t) = \theta_0 + \theta_{soc}\left[SOC_{max} - SOC(t)\right] + \theta_p \frac{\left[\hat{c}^{H}_{max}(t) - c_{el}(t)\right]_+}{c_{ref}} \quad (11)$$

where c_{ref} is a reference electricity price determined from the calibration data. A lower state of charge or a larger anticipated price spread increases $\Theta(t)$, so stronger evidence of persistent surplus is required before electricity is diverted from the battery to P2G.

3.3 Soft BESS–P2G split

$$\rho_{P2G}(t) = \{0,\ R(t) \leq \Theta(t),\ min\left\{\rho_{max}, \frac{R(t)-\Theta(t)}{R(t)}\right\},\ R(t) > \Theta(t), \quad (12)$$

The fraction $\rho_{P2G}(t)$ of the current post-HP surplus is allocated initially to P2G, while the remaining surplus is assigned to BESS charging. If either device reaches its power or energy limit, the residual electricity is reassigned to the other device before curtailment is considered. The resulting policy therefore implements a soft allocation priority rather than a permanent reversal of the BESS and P2G order. The online computation consists of a short weighted forecast aggregation, a threshold update, and an allocation calculation. No optimization problem is solved during real-time operation.

3.4 Independent calibration

Hyperparameters are selected using an independent full-year synthetic realization reserved exclusively for calibration. The candidate forecast horizons are $H \in \{3, 6, 12\}$ h. The candidate values for the base threshold are $\theta_0 \in \{0.60, 0.90\}$, while $\theta_{soc} \in \{0.45, 0.90\}$ and $\theta_p \in \{0.30, 0.65\}$. The maximum P2G allocation fraction is fixed at $\rho_{max} = 0.80$. A controlled relative forecast-error level of 10% is included during calibration. The calibration objective is

$$J = C_{op} + \lambda_{CO_2} E_{CO_2} + \lambda_{cur} E_{cur}, \qquad \lambda_{CO_2} = 80\ EUR/t, \quad \lambda_{cur} = 25\ EUR/MWh \quad (13)$$

Calibration selects a 12 h forecast horizon with $\theta_0 = 0.60$, $\theta_{soc} = 0.45$, $\theta_p = 0.30$, and $\rho_{max} = 0.80$. The reference electricity price is $c_{ref} = 76.80$ EUR/MWh. These values are fixed before all subsequent synthetic tests, stress scenarios, capacity scans, and transfer-validation experiments.

4. Experimental Design and Validation Protocol

4.1 Reproducible synthetic benchmark

The synthetic benchmark represents one complete year at hourly resolution, yielding 8760 time steps. Electrical demand follows a weekday and shift-dependent industrial profile. PV generation follows a seasonal solar envelope with correlated cloud variability, while wind generation is represented by a winter-enhanced autoregressive capacity-factor process. Heat demand combines an industrial baseline with a temperature-dependent heating component referenced to 18°C. Electricity prices follow a transparent time-of-use structure with an additional scarcity component. Independent stochastic realizations are used for calibration and testing so that the evaluation data do not contribute to parameter selection.

Table 1: Main device and economic parameters.

Parameter	Value
Time step	1 h
BESS energy / power	10 MWh / 2.5 MW
BESS charge/discharge efficiency	0.95 / 0.95
SOC bounds	0.10–0.90
BESS throughput cost	4 EUR/MWh throughput
CHP maximum electrical power	3.2 MW
CHP electrical / thermal efficiency	0.36 / 0.45
HP maximum heat output	5.0 MW_{th}
HP COP	2.25–4.45
P2G maximum electrical power	2.0 MW
P2G SNG efficiency / heat ratio	0.60 / 0.12
P2G operating cost	2 EUR/MWh_e
GB efficiency	0.90
Natural-gas price	52 EUR/MWh
Natural-gas / grid emission factors	0.202 / 0.34 tCO_2/MWh

The principal physical and economic settings used in the synthetic benchmark are listed in Table 1. Unless otherwise stated, the synthetic test-year FARSA forecasts use an independent 10% relative-error realization. The static rule does not use forecast information.

To avoid bias associated with an arbitrary initial BESS state, each rule controller is evaluated under a periodic steady-state condition. The annual sequence is repeated until the difference between the terminal and initial state of charge satisfies $|SOC_{end} - SOC_{start}| < 10^{-6}$. Gas use is evaluated over an open-network annual settlement boundary in which gross CHP and gas-boiler consumption is offset by annual SNG production to obtain the net external fossil-gas equivalent. This accounting convention

avoids introducing an unobserved gas-storage trajectory and is applied consistently to all controllers and optimization references.

$$E_{gas}^{net} = \left\{0, \sum_t [E_{CHP}(t) + E_{GB}(t) - \sum_t E_{SNG}(t)\right\}$$
$$C_{op} = c_g E_{gas}^{net} + \sum_t \left[c_{el}(t) P_{grid}(t)\Delta t + c_B\left(P_{ch}(t) + P_{dis}(t)\right)\Delta t + c_{P2G} P_{P2G}(t)\Delta t\right] \quad (14)$$

$$E_{CO2} = e_g E_{gas}^{net} + e_{grid} \sum_t P_{grid}(t)\Delta t \quad (15)$$

4.2 Scenario design and blocked inference

Six operating conditions are evaluated: the baseline case, a 25% increase in renewable capacity, a 20% reduction in renewable capacity, a high-demand case with 10% higher electrical demand and 15% higher heat demand, a winter-stress case with ambient temperature reduced by 4°C and the thermal variables recalculated, and a volatile-renewables case with stronger correlated generation variability. Ten independent stochastic realizations are generated. Within each paired comparison, the static rule and FARSA are evaluated on the same exogenous trajectory. The 60 condition-realization combinations are reported descriptively, but conditions derived from the same stochastic realization are not treated as independent inferential units. The six condition effects are first averaged within each realization, yielding ten independent blocked observations.

$$\bar{\Delta}_s = \frac{1}{6} \sum_{c=1}^{6} \Delta_{s,c}, \qquad s = 1, \ldots, 10 \quad (16)$$

Two-sided one-sample t tests and Wilcoxon signed-rank tests are then applied to the ten blocked observations. Scenario-level 95% confidence intervals use the Student's t critical value $t_{0.975,9} = 2.262$.

4.3 Objective-consistent perfect-foresight optimization

A system-level perfect-foresight linear program (PF-LP) is used only as an idealized reference. Let $S(t) = [P_{RES}(t) - P_{load}(t)]_+$ denote renewable surplus and let $D(t) = [P_{load}(t) - P_{RES}(t)]_+$ denote the corresponding electrical deficit. The PF-LP uses the same physical energy pathways as the rule-based simulator. Renewable electricity first supplies the contemporaneous electrical demand. Any remaining surplus can be used by the HP, stored in the BESS, converted through P2G, or curtailed. Electrical deficits can be supplied by BESS discharge, CHP generation, or grid import. Usable CHP and P2G heat are allowed to remain below their available heat output, so excess heat can be rejected rather than being forced into the thermal balance. This formulation maintains consistency with the rule-based simulator.

$$P_{HP,RES} + P_{ch} + P_{P2G} + P_{cur} = S(t) \quad (17)$$
$$P_{dis} + P_{CHP,L} + P_{grid} = D(t) \quad (18)$$
$$COP\left(P_{HP,RES} + P_{CHP,HP}\right) + Q_{CHP,use} + Q_{P2G,use} + \eta_{GB} F_{GB} = Q_{dem} \quad (19)$$
$$0 \le Q_{CHP,use} \le \frac{\eta_h}{\eta_e}\left(P_{CHP,L} + P_{CHP,HP}\right), \qquad 0 \le Q_{P2G,use} \le \kappa_h P_{P2G} \quad (20)$$

The PF-LP constrains total CHP electrical output by the rated CHP capacity and applies the same HP thermal limit, BESS power and state-of-charge bounds, and conversion efficiencies as the rule-based simulator. Because the hourly model does not include start-up costs, minimum stable output, or ramping constraints, binary unit-commitment variables would not represent additional physical behavior. The reference problem is therefore formulated as a continuous linear program. BESS dynamics use a cyclic annual boundary so that the terminal state equals the initial state, while the cycle level remains free within the admissible state-of-charge range. Objective consistency is preserved by solving separate reference problems. One minimizes annual operating cost, denoted C^*, while the second minimizes renewable curtailment subject to an operating-cost limit of $C_{op} \leq 1.01C^*$.

4.4 Measurement-driven transfer validation using Honda facility data

The transfer validation uses public measurements from a medium-sized industrial and office facility operated by Honda Research and Development (R&D) Europe in Offenbach am Main, Germany, covering 2018–2023 (Engel et al., 2025a). The public repository includes electrical, thermal, cooling, and on-site meteorological measurements at multiple temporal resolutions, including hourly aggregates (Engel et al., 2025b). The facility contains a 749 kWp photovoltaic system and a 199 kW_{el} gas-fired CHP unit. The transfer evaluation uses the hourly electrical, thermal, and meteorological measurements. The electrical metering records signed grid exchange together with on-site PV and CHP generation. A preliminary data-quality assessment showed that PV measurements are unavailable for 4,295 hours in 2019 and become continuously available from 29 June 2019. To avoid imputing an unobserved PV trajectory, the earlier validation window is restricted to 6 July–31 December 2019 after allowing one week of historical observations for causal forecasting. The complete 2023 calendar year is used as the primary full-year measured test because all required variables are jointly available throughout that period. Facility electrical demand is reconstructed by reconciling the signed grid-exchange measurements with metered PV and CHP generation according to the source metering convention. Historical CHP generation is used only for reconstructing the original facility demand and is not reintroduced as exogenous generation in the counterfactual dispatch. Total measured heat production is used as an hourly proxy for thermal demand, while ambient temperature is taken directly from the on-site meteorological observations. Wind generation is set to zero because no on-site wind generation is present in the measured facility.

Virtual BESS and P2G ratings are transferred from the synthetic benchmark without tuning on the measured validation trajectories. The BESS power rating is set to 37.8% of the site's 95th-percentile electrical demand, with an energy capacity corresponding to four hours at rated power. The P2G electrical rating is set to 30.2% of the same demand statistic. The CHP rating is fixed at the documented site value of 0.199 MW, and the HP thermal rating is set to 64.6% of the 95th-percentile thermal-demand proxy. For the 2023 test year, these transfer rules give a BESS energy capacity of 0.690 MWh, a BESS power rating of 0.172 MW, a P2G rating of 0.138 MW, and an HP thermal rating of 0.327 MW_{th}. Accordingly, this stage is a counterfactual replay test driven by measured exogenous trajectories, not a field trial of physical BESS or P2G equipment at the Honda facility.

Because the public facility measurements do not include a site electricity-price series, both controllers are evaluated under the same deterministic time-of-use benchmark tariff for secondary economic comparison. The base tariff is 55 EUR/MWh, with a 25 EUR/MWh increment during 08:00–12:00 and 17:00–21:00 and a 7 EUR/MWh weekday increment. Curtailment and physical energy-flow metrics are

therefore treated as the primary transfer-validation outcomes. Operating cost is interpreted only as a tariff-dependent model output rather than as an observed market-cost measure.

4.5 Causal external forecasting protocol

No future measurement is used by the controller. The 12 h forecasts are generated with a causal seasonal-naive model that uses only historical observations available at the decision time:

$$\hat{P}_L(t+k) = 0.5P_L(t+k-24) + 0.5P_L(t+k-168) \quad (21)$$

$$\hat{P}_{PV}(t+k) = 0.7P_{PV}(t+k-24) + 0.3P_{PV}(t+k-168) \quad (22)$$

$$\hat{Q}_{dem}(t+k) = 0.5Q_{dem}(t+k-24) + 0.5Q_{dem}(t+k-168) \quad (23)$$

Ambient temperature is forecast using the same daily and weekly seasonal mixture before conversion to the forecast heat-pump coefficient of performance. The benchmark tariff is known deterministically from calendar time. Forecast accuracy is evaluated using mean absolute error (MAE), root mean square error (RMSE), and weighted absolute percentage error (WAPE) over all target points in the rolling 12 h horizons. WAPE is computed as the sum of absolute forecast errors divided by the sum of the corresponding observed magnitudes. External transfer is evaluated at the measured PV capacity and under counterfactual capacity increases of 25% and 50% while preserving the measured temporal generation profile. These expanded-capacity cases are scenario analyses and are not interpreted as additional measured operating years.

Figure 2 shows a representative week of reconstructed electrical demand, measured PV generation, and the measured heat-production proxy. The observed daily variation confirms that the external evaluation is driven by facility measurements rather than by the synthetic profile generator.

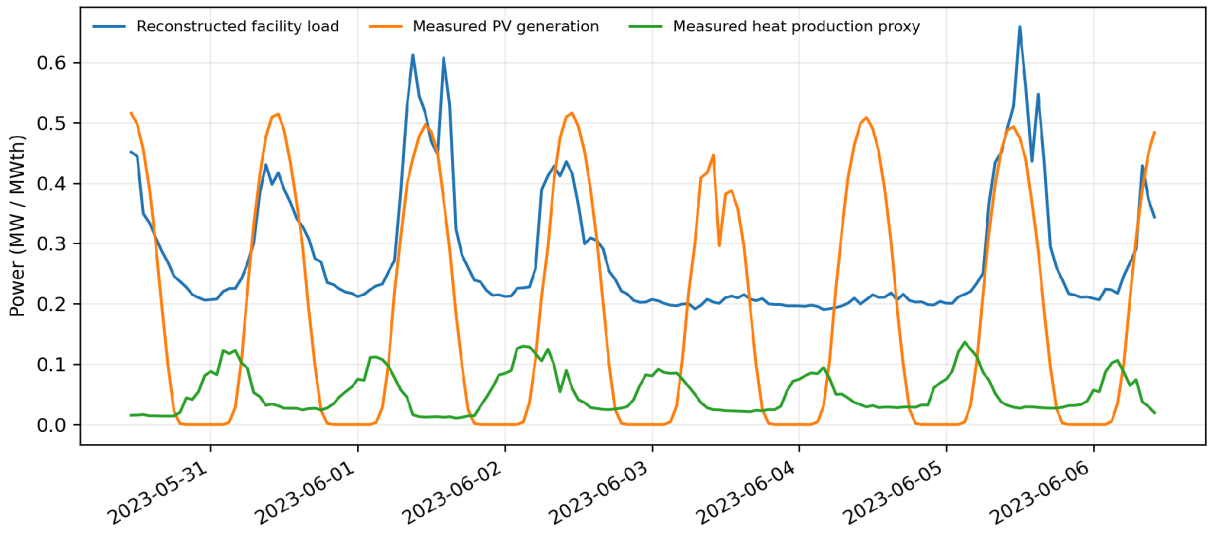


Figure 2. Representative week of the 2023 Honda facility measurements used for transfer validation.

5. Results

5.1 Synthetic base case

Table 2: Annual synthetic-benchmark results.

Strategy	Net gas (GWh)	GB gas (GWh)	HP heat (GWh)	P2G electricity (GWh)	Curtailment (MWh)	CO_2 (t)	Cost (M€)
Baseline rule	36.527	22.890	9.011	0.771	237.83	7391.0	1.9109
Static coordinated rule	32.015	12.128	15.885	0.771	237.83	6479.6	1.6763
FARSA	31.974	12.072	15.907	0.852	173.74	6471.3	1.6742

Table 2 compares the baseline rule, the static coordinated rule, and FARSA under the same synthetic test year and physical parameters.

The static coordinated rule reproduces the key cross-device mechanism embedded in the DRL-derived baseline controller: GB gas use falls from 22.890 to 12.128 GWh while CHP gas use increases, because additional CHP electricity and heat jointly displace boiler heat through the CHP–HP pathway. Relative to the baseline rule, the static coordinated controller reduces net fossil gas by 12.35% and operating cost by 12.28%.

FARSA then provides a smaller but physically targeted incremental gain. Curtailment falls from 237.83 to 173.74 MWh, a reduction of 26.95%. P2G electricity rises from 770.60 to 852.41 MWh, whereas BESS charging decreases slightly from 819.20 to 801.48 MWh. Operating cost, net fossil gas, and CO_2 decrease only 0.126%, 0.128%, and 0.128%, respectively. This pattern is consistent with the intended role of FARSA: it corrects surplus-timing mismatch rather than replacing system-wide dispatch.

The normalized annual comparison in Figure 3 makes the scale separation clear: the static CHP–HP rule delivers the dominant system-level saving, whereas FARSA adds a targeted curtailment reduction on top of that rule.

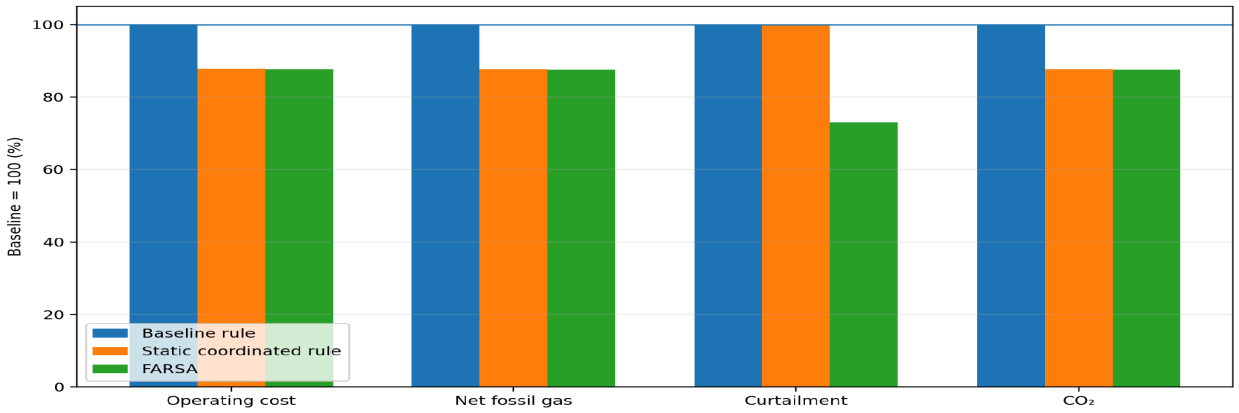


Figure 3. Normalized annual KPI comparison in the synthetic benchmark.

5.2 Trigger mechanism and forecast-error sensitivity

FARSA activates early P2G splitting during 1,003 of 8,760 hours (11.4%). It therefore leaves the original BESS-first rule unchanged during most hours. During persistent renewable events, early P2G operation prevents the BESS from reaching its SOC ceiling too soon, creating a complementary pattern in which P2G absorbs sustained surplus and BESS retains high-power peak-shaving headroom.

Figure 4 illustrates the trigger mechanism over the 168-h window with the largest number of FARSA activations. All displayed quantities are normalized: BESS state of charge, P2G utilization relative to rated power, the FARSA split fraction, and a binary trigger state that equals one when $R(t) > \Theta(t)$.

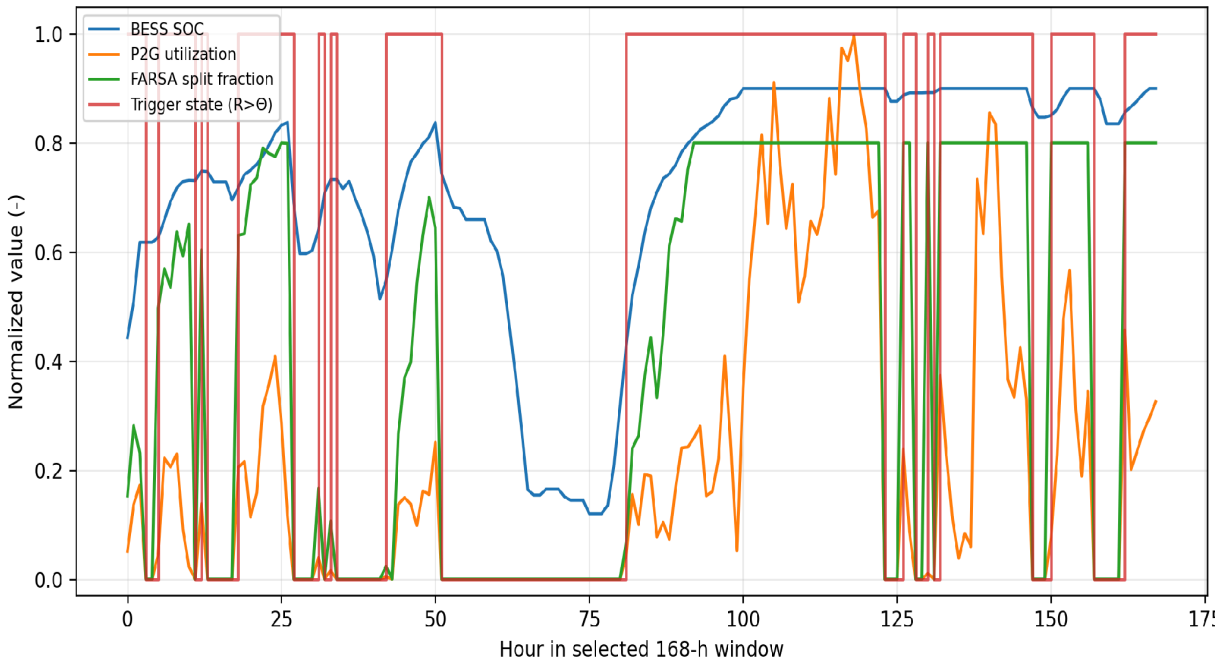


Figure 4. Representative week with frequent FARSA activation.

Controlled synthetic forecast-error experiments perturb future load, renewable generation, heat demand, COP, and price by zero-mean relative noise. These experiments are not presented as a trained forecasting model. They are used only to test sensitivity to forecast imperfection. Curtailment remains below the static rule throughout the tested 0–30% noise range, while cost changes are not strictly monotonic because forecast error can shift P2G triggers in either direction.

As shown in Figure 5, curtailment remains below the static-rule level throughout the controlled 0–30% error range. The secondary axis is used for the much smaller cost and CO_2 changes so that these effects are not visually masked by the larger curtailment response.

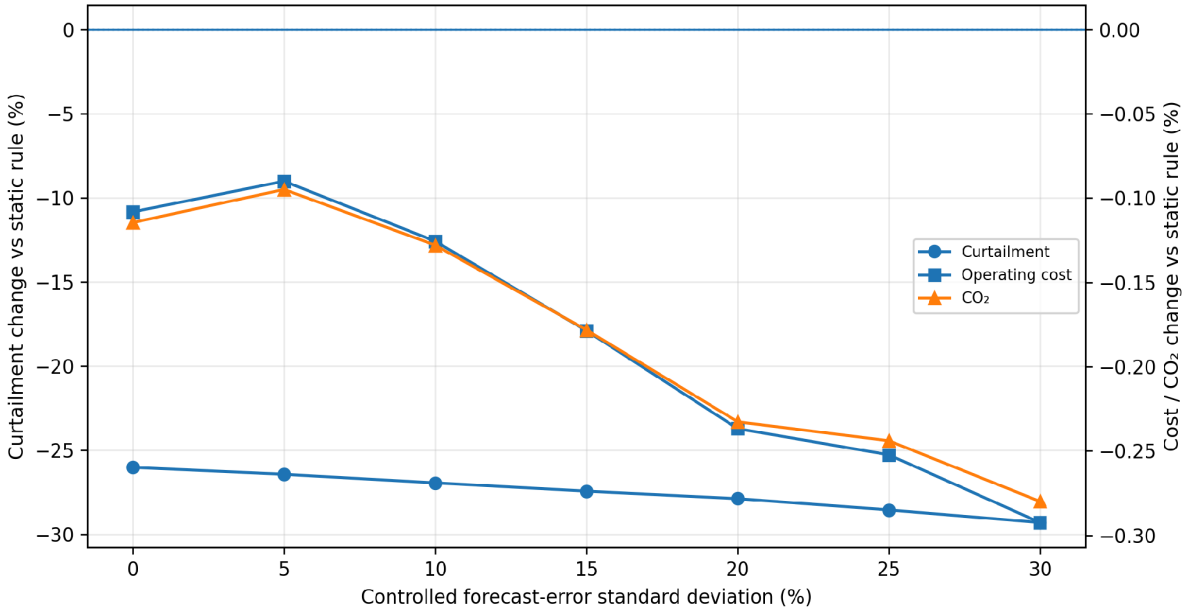


Figure 5. Sensitivity of FARSA to controlled short-horizon forecast errors.

5.3 Multi-scenario and blocked statistical validation

Table 3: FARSA relative to the static rule across ten stochastic realizations (mean ± SD).

Scenario	Cost Δ%	Net gas Δ%	Curtailment Δ %	CO_2 Δ%
Baseline	-0.120 ± 0.031	-0.122 ± 0.031	-30.33 ± 10.23	-0.121 ± 0.031
High renewable	-0.425 ± 0.050	-0.454 ± 0.052	-10.28 ± 1.47	-0.452 ± 0.052
High demand	-0.060 ± 0.018	-0.060 ± 0.017	-38.14 ± 10.52	-0.060 ± 0.018
Low renewable	-0.009 ± 0.009	-0.008 ± 0.009	-68.41 ± 22.90	-0.008 ± 0.009
Volatile renewable	-0.131 ± 0.032	-0.134 ± 0.033	-22.35 ± 8.72	-0.133 ± 0.033
Winter stress	-0.093 ± 0.027	-0.094 ± 0.028	-31.09 ± 9.52	-0.094 ± 0.028

Table 3 reports scenario-wise descriptive statistics across the ten stochastic realizations. Negative Δ% denotes a reduction relative to the static coordinated rule.

Table 4: Blocked inferential statistics across independent stochastic realizations ($n = 10$).

Metric	Blocked mean Δ%	95% CI	Wilcoxon p	Holm-adjusted p
Operating cost	-0.140	[-0.151, -0.129]	0.0020	0.0078
Net fossil gas	-0.145	[-0.156, -0.134]	0.0020	0.0078
Curtailment	-33.435	[-38.901, -27.969]	0.0020	0.0078
CO_2	-0.145	[-0.156, -0.134]	0.0020	0.0078

Table 4 reports inference based on the ten independent blocked effects rather than on the 60 correlated condition–realization combinations. Because the inferential sample contains only ten independent stochastic realizations, the Wilcoxon signed-rank test is used as the primary significance test. All four tests remain significant after Holm correction, with an adjusted value of $p = 0.0078$.

After blocking by stochastic realization, the mean reduction is 33.43% for curtailment and 0.140% for operating cost. The Wilcoxon signed-rank test gives $p = 0.0020$ for both metrics, indicating a consistent direction of paired change across the ten independent realizations. Statistical significance should not be confused with operational magnitude: the economic effect remains small in percentage terms, whereas the curtailment reduction is substantially larger and more directly associated with the proposed allocation mechanism.

Figure 6 provides the 60 paired condition–realization curtailment outcomes only as a descriptive visualization. The inferential unit remains the independent stochastic realization as specified above.

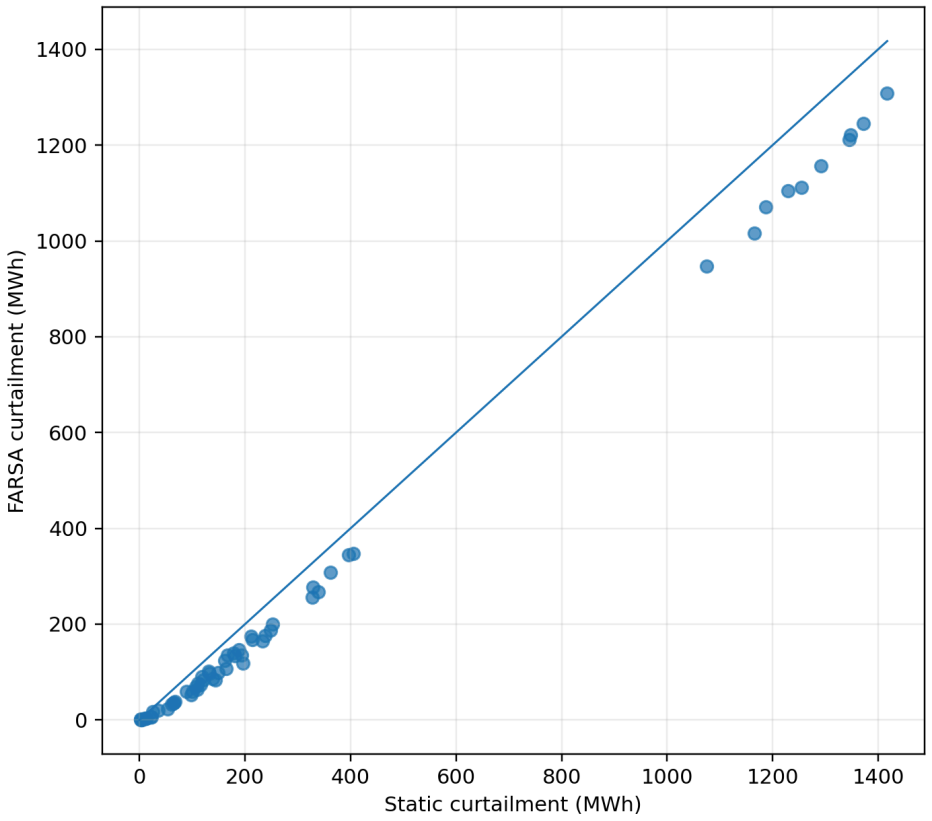


Figure 6. Paired curtailment outcomes across condition–realization combinations.

5.4 Capacity scans and applicability boundary

Capacity scans vary one parameter at a time while holding the baseline exogenous year, the 10% forecast-error realization, and all other parameters fixed. Consequently, the nominal scan point, defined by a renewable-capacity multiplier of 1.0, a 10 MWh/2.5 MW BESS, and a 2 MW P2G unit, reproduces the base-case comparison between FARSA and the static coordinated rule. Table 5 summarizes the scan

results and clarifies when a priority adjustment can matter. At only 0.6× renewable capacity, virtually no surplus exists and FARSA is effectively inactive. As renewable capacity grows, absolute curtailment rises and the relative curtailment reduction from FARSA becomes smaller because combined BESS and P2G power limits eventually dominate. Increasing BESS energy capacity from 5 to 20 MWh changes timing flexibility but does not produce a monotonic economic gain. Increasing P2G power from 0.5 to 4 MW progressively increases the relative curtailment reduction, while the cost improvement peaks at intermediate P2G ratings and then declines. FARSA therefore addresses a temporal allocation problem. It cannot compensate for fundamentally inadequate flexibility capacity.

Table 5: One-factor-at-a-time capacity-scan effects of FARSA relative to the static rule.

Parameter varied	Setting	Cost Δ%	Curtailment Δ%
Renewable-capacity multiplier	0.6	0.000	—
	0.8	-0.016	-69.09
	1	-0.126	-26.95
	1.2	-0.300	-10.46
	1.4	-0.715	-5.06
	1.6	-1.099	-1.73
BESS energy (MWh)	5	-0.115	-19.47
	7.5	-0.155	-24.37
	10	-0.126	-26.95
	12.5	-0.099	-27.38
	15	-0.145	-27.67
	20	-0.098	-26.21
P2G power (MW)	0.5	-0.141	-9.79
	1	-0.154	-15.80
	1.5	-0.152	-22.51
	2	-0.126	-26.95
	2.5	-0.101	-29.03
	3	-0.078	-30.84
	4	-0.045	-33.75

In Table 5, "—" denotes an undefined percentage change because the static-rule curtailment is effectively zero at the 0.6× renewable setting. It is not a missing simulation result.

5.5 Perfect-foresight reference and fairness interpretation

Table 6: Rule controllers and objective-consistent perfect-foresight references.

Controller/reference	Cost (M€)	Net gas (GWh)	Curtail. (MWh)	CO_2 (t)	Grid import (MWh)
Static coordinated rule	1.6763	32.015	237.83	6479.6	36.8
FARSA	1.6742	31.974	173.74	6471.3	36.8
PF-LP cost optimum	1.3174	17.808	132.59	5119.3	4476.5
PF-LP minimum curtailment ($C_{op} \leq 1.01C^{*}$)	1.3305	17.546	127.21	5135.5	4680.2

Table 6 compares the two rule controllers with the objective-consistent PF-LP references under the same physical conversion model and annual gas-accounting boundary.

The cost-optimal perfect-foresight reference achieves an annual operating cost of 1.3174 M€, compared with 1.6742 M€ for FARSA. The FARSA value is therefore 27.09% above the idealized lower-bound reference. This gap reflects both perfect knowledge of the full-year trajectory and system-wide co-optimization of all controllable devices. It should not be interpreted as the isolated performance cost of the BESS–P2G allocation rule.

The cost-optimal solution is not used as a surrogate optimum for renewable curtailment. A separate reference minimizes curtailment subject to the operating-cost constraint $C_{op} \leq 1.01C^{*}$, yielding 127.21 MWh. FARSA produces 173.74 MWh of curtailment, which is 36.58% higher than this objective-consistent reference. The perfect-foresight solutions also rely on substantially larger grid imports, showing that system-level cost optimization can select an operating pathway that differs materially from the interpretable rule-based strategies under the assumed prices and emission factors.

The normalized comparison in Figure 7 emphasizes that the perfect-foresight references achieve their lower cost primarily through system-wide re-dispatch, including much larger grid imports, rather than through the BESS–P2G split alone.

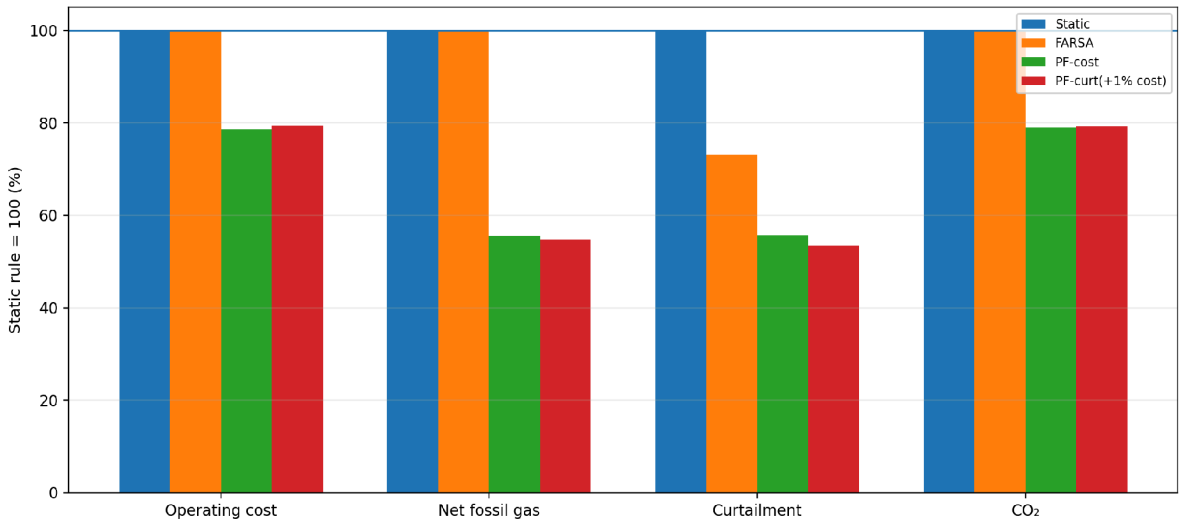


Figure 7. Rule controllers versus objective-consistent perfect-foresight linear-program references.

5.6 Transfer evaluation on the Honda industrial facility

5.6.1 Data quality and forecast accuracy

A data-quality assessment identified a substantial gap in the 2019 PV record. Measurements are unavailable for 4,295 hourly observations and become continuously available from 29 June 2019. No values are imputed. The earlier validation window therefore covers 6 July–31 December 2019, which also provides the historical context required by the daily and weekly seasonal lags. The complete 2023

calendar year is used as the primary full-year measured test because the electrical, PV, thermal, and meteorological measurements are jointly available throughout that year.

Table 7: Accuracy of the causal seasonal-naive 12 h forecasts for the Honda facility measurements.

Window	Forecast variable	MAE	RMSE	WAPE
6 Jul–31 Dec 2019	Electrical demand	0.0400	0.0576	13.76%
6 Jul–31 Dec 2019	PV generation	0.0047	0.0105	35.76%
6 Jul–31 Dec 2019	Thermal-demand proxy	0.0714	0.0928	29.63%
2023 full year	Electrical demand	0.0383	0.0604	14.59%
2023 full year	PV generation	0.0251	0.0549	33.53%
2023 full year	Thermal-demand proxy	0.0567	0.0816	29.08%

Table 7 reports forecast accuracy for both measured test windows. MAE and RMSE are expressed in MW for electrical demand and PV generation and in MW_{th} for the thermal-demand proxy. WAPE is dimensionless.

The seasonal-naive predictor is deliberately parsimonious and is not optimized for forecasting performance. For the complete 2023 year, WAPE is 14.59% for electrical demand, 33.53% for PV generation, and 29.08% for the thermal-demand proxy. This level of forecast error provides a measurement-driven assessment of the FARSA threshold logic without relying on perfect future information.

5.6.2 Transfer results

Table 8: Measurement-driven Honda transfer evaluation with fixed FARSA parameters.

Window	PV scale	Static curtailment (MWh)	FARSA curtailment (MWh)	Curtailment Δ%	Cost Δ %	Net gas Δ%	CO_2 Δ %	Active hours
6 Jul–31 Dec 2019	1.00×	0.00	0.00	0.00	0.000	0.000	0.000	0
6 Jul–31 Dec 2019	1.25×	0.00	0.00	0.00	0.000	0.000	0.000	0
6 Jul–31 Dec 2019	1.50×	0.00	0.00	0.00	0.000	0.000	0.000	0
2023	1.00×	3.96	2.23	-43.75	-0.012	-0.014	-0.012	134
2023	1.25×	18.88	14.79	-21.67	0.019	0.019	0.020	390
2023	1.50×	50.60	42.96	-15.10	0.041	0.029	0.045	630

Table 8 summarizes the measurement-driven transfer results obtained with all FARSA parameters fixed before the Honda measurements are introduced. Negative percentage changes denote reductions relative to the static coordinated rule.

During 6 July–31 December 2019, no post-HP renewable curtailment occurs even when the measured PV profile is scaled to 150% of its observed capacity. FARSA therefore remains inactive and reproduces the static-rule trajectory. This result defines an important operating boundary: the adaptive split does not alter dispatch when persistent surplus is absent.

For the complete 2023 record at the measured PV capacity, renewable curtailment decreases from 3.96 MWh under the static rule to 2.23 MWh under FARSA, corresponding to a 43.75% reduction. P2G electricity use increases by 13.66%, while BESS charging decreases by 0.74%. Annual operating cost decreases by 0.012%, net fossil-gas use by 0.014%, and CO_2 emissions by 0.012% under the benchmark tariff. The dominant transferred benefit is therefore improved absorption of renewable surplus rather than a material economic gain.

When PV capacity is increased by 25% and 50%, FARSA continues to reduce curtailment by 21.67% and 15.10%, respectively. However, annual operating cost increases by 0.019% and 0.041%, while CO_2 emissions increase by 0.020% and 0.045%. Although these changes are small, they show that a rule calibrated for surplus absorption does not guarantee simultaneous improvement in every objective as renewable penetration changes. FARSA should therefore be interpreted as a targeted curtailment-management enhancement, with supervisory multi-objective optimization becoming more appropriate when economic or emission trade-offs are material.

Figure 8 visualizes the curtailment reduction across the measured and expanded-PV cases, whereas Figure 9 shows the much smaller secondary cost, gas, and CO_2 changes. Reading the two figures together prevents the large curtailment effect from being mistaken for a similarly large economic effect.

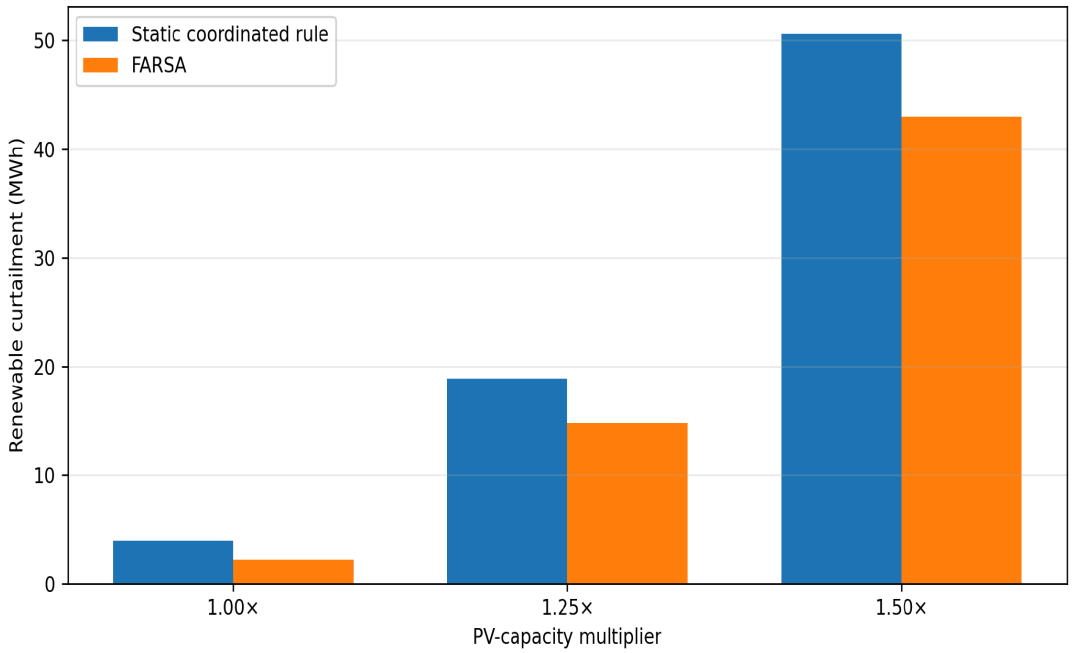


Figure 8. Honda 2023 curtailment under measured and counterfactual PV-capacity scenarios.

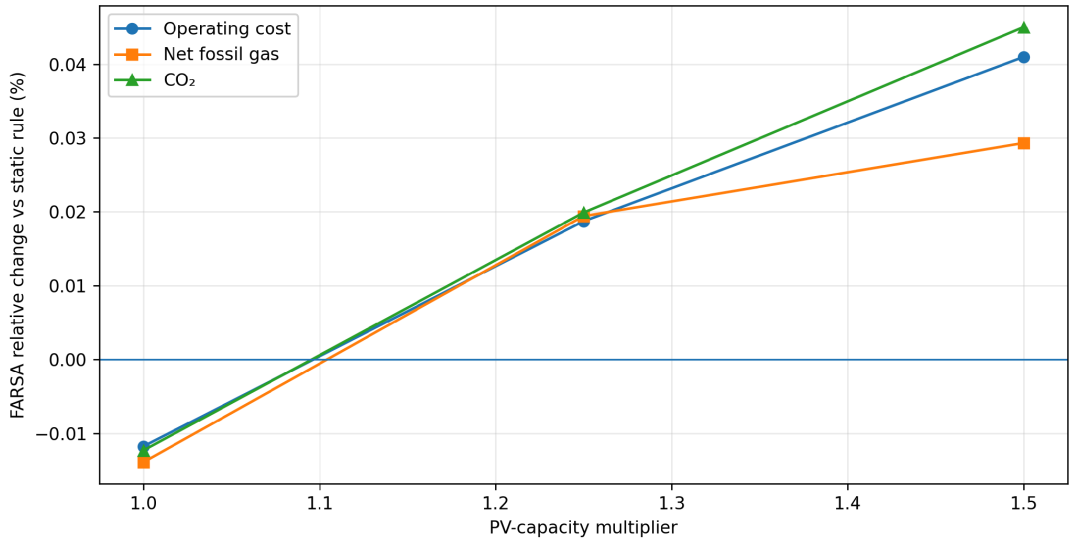


Figure 9. Honda 2023 secondary cost, gas-use, and CO_2 changes relative to the static rule.

6. Discussion and Managerial Implications

6.1 Mechanistic interpretation of FARSA

The results support a specific mechanistic interpretation of FARSA. The method modifies the timing of P2G participation in renewable-surplus absorption while preserving the system topology and the previously identified CHP–HP cooperative-heating mechanism. The synthetic benchmark shows that this timing adjustment can substantially reduce curtailment. The measurement-driven transfer test shows that the same behavior is retained when the rule is replayed on measured industrial demand and PV trajectories with persistent surplus. At higher PV penetration, however, the economic effect becomes negligible or slightly adverse. FARSA is therefore best interpreted as a focused surplus-allocation refinement rather than as a general system-wide optimization method.

6.2 Managerial and operational implications

For plant operators, the principal management advantage is transparency. FARSA can be implemented within a supervisory control procedure using a limited set of physically interpretable quantities: forecast post-HP surplus, remaining battery headroom, state of charge, and anticipated electricity-price value. The resulting activation condition can be inspected retrospectively and constrained directly by device operating limits. This structure differs from a neural control policy whose individual actions are not readily attributable to a small number of explicit physical conditions.

The measured-data transfer test also delineates conditions under which adaptive splitting is unlikely to provide material benefit. When renewable surplus is rare, as observed during the 2019 validation window, FARSA remains inactive. At the opposite extreme, if renewable penetration is sufficiently high that both BESS and P2G frequently reach their power limits, additional flexibility capacity becomes more important than allocation-priority refinement. Between these regimes, FARSA can reduce curtailment without requiring an online optimization solver. The broader operational implication is that rule refinement is appropriate when timing is the dominant bottleneck, whereas capacity investment or

system-level optimization becomes more important when hard flexibility limits or multi-objective trade-offs dominate.

6.3 Limitations

Five limitations should be noted. First, the hourly model omits CHP start-up costs, minimum stable output, ramping constraints, P2G minimum load, nonlinear BESS degradation, and thermal-network dynamics. Second, the Honda facility does not contain the virtual BESS and P2G capacities introduced in the counterfactual analysis. The transfer evaluation therefore tests the controller on measured exogenous trajectories rather than demonstrating field actuation of those devices. Third, measured total heat production is used as a proxy for thermal demand. Fourth, the public facility measurements do not include electricity prices, so the reported external cost is based on a common benchmark tariff and should not be interpreted as observed market expenditure. Fifth, the perfect-foresight linear program has access to the complete annual trajectory and therefore provides an idealized lower-bound reference rather than a matched-information online competitor. A future rolling-horizon optimization using the same 12 h forecasts would permit a more direct assessment of the performance loss associated with rule simplification.

7. Conclusion

This paper extends an interpretable coordinated-rule energy-management framework with a focused forecast-aware BESS–P2G surplus-allocation mechanism. By consistently defining post-HP surplus, input-side BESS headroom, independent calibration, and blocked statistical inference, FARSA reduces synthetic-benchmark curtailment by 26.95% relative to the static coordinated rule while changing annual operating cost and fossil-gas use by approximately one tenth of one percent. Across six operating conditions and ten independent stochastic realizations, the directions of the curtailment and cost effects remain statistically consistent.

Measurement-driven transfer evaluation using the public Honda industrial-facility data provides a more stringent assessment than synthetic testing alone. During 6 July–31 December 2019, no relevant post-HP surplus occurs and FARSA remains inactive. For the complete 2023 record at the measured PV capacity, FARSA reduces curtailment by 43.75% while changing benchmark-tariff operating cost by only 0.012%. Under 25% and 50% PV-capacity increases, the method continues to reduce curtailment but introduces very small cost and emission penalties. FARSA should therefore be viewed as a transparent surplus-absorption refinement rather than as a universally Pareto-improving controller.

The objective-consistent perfect-foresight analysis further separates rule performance from optimization potential and avoids using a cost-optimal dispatch as a surrogate curtailment optimum. Taken together, the synthetic and measurement-driven evidence supports a staged control strategy in which complex learning or optimization tools may be used offline to explore coordination opportunities, deployable behavior is expressed through inspectable operating rules, FARSA is applied when surplus timing is the dominant residual limitation, and rolling optimization or capacity planning is adopted when multi-objective trade-offs or hard flexibility constraints become dominant.

Data and Code Availability

The synthetic benchmark generator and analysis scripts used for the reported experiments are available from the corresponding author upon reasonable request. The original Honda facility measurements are

not redistributed and remain publicly available from Dryad under DOI 10.5061/dryad.73n5tb363 (Engel et al., 2025b).

Acknowledgement

The authors wish to thank State Grid Fujian Electric Power Economic and Technological Research Institute for their support.

Conflict of Interest

The authors declare that there is no conflict of interest regarding the publication of this article.

References

1. Abedi, S., Yoon, S. W., & Kwon, S. (2022). Battery energy storage control using a reinforcement learning approach with cyclic time-dependent Markov process. *International Journal of Electrical Power & Energy Systems, 134*, 107368.
2. Badami, M., & Fambri, G. (2019). Optimizing energy flows and synergies between energy networks. *Energy, 173*, 400–412.
3. Biermann, T., & Bocklisch, T. (2026). Hierarchical energy management for hybrid large-scale battery storage and power-to-gas systems in multi-use PV park applications. *Journal of Energy Storage, 154*, 121158.
4. Engel, J., Castellani, A., Wollstadt, P., et al. (2025a). A real-world energy management dataset from a smart company building for optimization and machine learning. *Scientific Data, 12*, 864. https://doi.org/10.1038/s41597-025-05186-3
5. Engel, J., Castellani, A., Wollstadt, P., et al. (2025b). A real-world energy management data set from a smart company building for optimization and machine learning. *Dryad Dataset*. https://doi.org/10.5061/dryad.73n5tb363
6. Fujimoto, S., van Hoof, H., & Meger, D. (2018). Addressing function approximation error in actor-critic methods. In *Proceedings of the 35th International Conference on Machine Learning* (Vol. 80, pp. 1587–1596).
7. Gillessen, B., Heinrichs, H. U., Stenzel, P., & Linssen, J. (2017). Hybridization strategies of power-to-gas systems and battery storage using renewable energy. *International Journal of Hydrogen Energy, 42*(19), 13554–13567. https://doi.org/10.1016/j.ijhydene.2017.03.163
8. Guo, C., Wang, X., Zheng, Y., et al. (2022). Real-time optimal energy management of microgrid with uncertainties based on deep reinforcement learning. *Energy, 238*, 121873.
9. Lillicrap, T. P., Hunt, J. J., Pritzel, A., et al. (2015). Continuous control with deep reinforcement learning. *arXiv preprint arXiv:1509.02971*.
10. Mancarella, P. (2014). MES (multi-energy systems): An overview of concepts and evaluation models. *Energy, 65*, 1–17.
11. Mohammadi, M., Noorollahi, Y., Mohammadi-Ivatloo, B., et al. (2017). Energy hub: From a model to a concept—A review. *Renewable and Sustainable Energy Reviews, 80*, 1512–1527.
12. Open Power System Data. (2020). *Data Package Time Series, Version 2020-10-06*. https://doi.org/10.25832/time_series/2020-10-06
13. Perera, A. T. D., & Kamalaruban, P. (2021). Applications of reinforcement learning in energy systems. *Renewable and Sustainable Energy Reviews, 137*, 110618.

14. Ruan, Y., Liang, Z., Qian, F., et al. (2023). Operation strategy optimization of combined cooling, heating, and power systems with energy storage and renewable energy based on deep reinforcement learning. *Journal of Building Engineering, 65*, 105682.
15. Ruhnau, O., Hirth, L., & Praktiknjo, A. (2019). Time series of heat demand and heat pump efficiency for energy system modeling. *Scientific Data, 6*, 189.
16. Sievers, J., & Blank, T. (2023). A systematic literature review on data-driven residential and industrial energy management systems. *Energies, 16*(4), 1688.
17. Sutton, R. S., & Barto, A. G. (2018). *Reinforcement Learning: An Introduction* (2nd ed.). MIT Press.
18. Zhou, S., et al. (2020). Combined heat and power system intelligent economic dispatch: A deep reinforcement learning approach. *International Journal of Electrical Power & Energy Systems, 120*, 106016.